CERN-ACC-NOTE-2020-0050

August 2020
luca.sabato@cern.ch
giovanni.iadarola@cern.ch

Numerical simulation studies on single-bunch instabilities driven by electron clouds at the LHC

L. Sabato, G. Iadarola and L. Mether

CERN, CH-1211 Geneva, Switzerland

Keywords: LHC, electron cloud, instabilities

Abstract

Instabilities driven by electron clouds in the LHC are studied by means of numerical simulations performed with the PyECLOUD-PyHEADTAIL suite. Particular attention is given to instabilities driven by e-cloud in the quadrupole magnets at injection energy, which are found to be the most critical case. The numerical parameters of the simulation (grids, number of macroparticles) are defined based on extensive convergence scans, which provide useful guidelines also for future simulation studies. The dependence of the beam stability on RF voltage, bunch intensity, transverse emittance, chromaticity and octupoles settings is investigated. The spectral properties of the unstable motion are analyzed. Simulations are also performed for less critical cases, namely instabilities driven by the quadrupoles at collision energy and instabilities driven by the dipoles at injection energy.

Contents

1 Introduction

During Run 2 (2015-2018) the Large Hadron Collider (LHC) has been operated with the nominal bunch spacing of 25 ns. In these conditions electron cloud (e-cloud) develops in the beam chambers, as witnessed by the large heat loads measured on the beam screens of the superconducting magnets [1–3].

The interaction of the circulating bunches with the e-cloud can trigger transverse head-tail instabilities, which have often been observed during LHC operation, especially at injection energy [4].

In this document we present a systematic study on these transverse instabilities and on their dependence on beam and machine configuration. The study is based on macro-particle (MP) simulations performed with the PyECLOUD-PyHEADTAIL suite [5]. The simulations, which have significant requirements in terms of computing resources and time, were performed on the High Performance Computing (HPC) cluster at INFN-CNAF (Bologna, Italy) and required several months of computing time.

Experimental observations at the LHC, as well as previous simulation studies, show that e-cloud instabilities are less critical at collision energy compared to injection energy due to the increased beam rigidity [6]. In spite of their modest length (they occupy only 7% of the accelerator length) the quadrupole magnets represent the main source of e-cloud instabilities in the LHC, due to the fact that their magnetic field gradient tends to favour the accumulation of electrons in the chamber (magnetic trapping [7]) and to concentrate a large electron density around the beam location. For these reasons, in this work particular attention is given to the study of instabilities driven by e-cloud in quadrupole magnets at injection energy. The simulation results presented in this document, have also been used to benchmark a recently developed linearized approach for the study of e-cloud instability using the Vlasov method, as described in Ref. [8].

The main beam and machine parameters used in the presented studies are summarized in Tab. 1. In case different parameters are considered, this will be explicitly stated.

Reliable simulations with these numerical tools require the correct definition of several numerical parameters (e.g. number of macroparticles, geometric discretization, time steps). In order to identify the correct settings to be used, we performed systematic numerical convergence scans, which also provide useful guidelines for future simulation studies.

This document is structured as follows: in Sec. 2 we will briefly describe the simulation setup; in Sec. 3 we will present the simulation studies on instabilities driven by e-cloud in the quadrupoles at injection energy, covering in particular the convergence studies for the definition of the numerical parameters for the simulations, the dependence on the RF voltage settings, the dependence on bunch intensity and transverse emittance, the effect of the transverse damper, chromaticity and octupoles; in Sec. 4 we will discuss instabilities driven by e-cloud in the quadrupoles at collision energy, including a set of numerical convergence scans for this scenario; and in Sec. 5 we will briefly discuss instabilities driven by e-cloud in the dipoles at injection energy.

Table 1: Main parameters for the considered simulation scenarios. For the parameters that differ between injection energy and collision energy the latter are indicated in parenthesis.

Beam energy [GeV]	450 (7000)
Bunch population, N_b [p/bunch]	1.2×10^{11}
R.m.s. bunch length, σ_b [cm]	9.0
R.m.s horizontal emittance (normalized) [μm]	2.5
R.m.s vertical emittance (normalized) [μm]	2.5
Ring circumference, ($2\pi R$) [km]	26.7
Horizontal beta function at the e-clouds, β_x [m]	92.7
Vertical beta function at the e-clouds, β_y [m]	93.2
Horizontal betatron tune, Q_x	62.27
Vertical betatron tune, Q_y	60.295
RF harmonic number	35640
RF voltage, V_{RF} [MV]	6 (12)
Momentum compaction factor, α	3.225e-04
Arc dipole field gradient [T]	0.54 (8.33)
Arc quadrupole gradient [T/m]	12.1 (188)
Fraction of the ring occupied by dipoles	66 %
Fraction of the ring occupied by quadrupoles	7 %

2 Description of the simulation setup

The numerical simulations described in this document are performed using the PyECLOUD-PyHEADTAIL suite [5]. The bunch is modelled by a set of MPs and the longitudinal and transverse beam dynamics are simulated using modules from the PyHEADTAIL code. As it is typically done in this kind of studies, the smooth approximation (constant beta functions) is used for the transverse dynamics and the longitudinal dynamics is lumped at a single location of the ring. The effect of chromaticity and octupoles on the betatron tunes can be taken into account. The effect of an ideal transverse feedback can also be included.

The e-cloud is modelled by a set of thin interactions installed along the ring. At each interaction the electron dynamics is simulated using the PyECLOUD code, based on the bunch distribution provided by PyHEADTAIL. For this purpose, the bunch is longitudinally sliced, each slice defining a time step for the simulation of the electron dynamics. For each slice, the forces generated by the bunch and by the electrons are computed using the Particle In Cell (PIC) method to solve a 2D Poisson problem [9, 10]. The electric field generated by the beam and by the electron themselves is taken into account for the simulation of the electron motion, while the electric field generated by the electron distribution alone defines the transverse kicks applied on the bunch MPs at each e-cloud interaction.

The e-cloud MPs at each interaction are initialized using the charge, position and momenta of MPs saved from PyECLOUD buildup simulations [11], performed with a rigid beam for the same scenario. The electron distribution from a single snapshot of the buildup simulation shows a significant numerical noise, due to the limited number of MPs. This would introduce numerical artifacts in the corresponding instability simulation. For this reason the MP set used in the instability simulation is obtained by merging MP sets from

several snapshots of the e-cloud at saturation, as obtained from the buildup simulation. Left-right and top-bottom symmetry of the distribution is also enforced by mirroring the MP distribution.

Parallel computing is regularly exploited by simulating different e-cloud interactions on different computing cores, using the PyPARIS parallelization layer [5]. Typically a number of cores equal to the number of e-cloud interactions is utilized.

Positions and statistical momenta of the bunch and of the slices are recorded by PyHEADTAIL at each revolution. To characterize the instability, a Fourier transform is applied to the position along the bunch at each turn and the instability growth rate is measured by applying an exponential fit on the most unstable spectral line (more detail on the spectral properties of the instabilities can be found in Sec. 3.5). Based on the computational time, we had to limit the simulation time window to 2×10^4 turns, which allows detecting instabilities with growth rates in the order of $0.5\,\mathrm{s}^{-1}$ (corresponding to a risetime of two seconds) or faster.

3 Instabilities driven by e-cloud in the quadrupoles at injection energy

As anticipated in Sec. 1, instabilities at injection energy driven by the e-cloud in the arc quadrupoles, which will be addressed in detail in this section, are particularly critical for the LHC operation. The stability properties are studied only in the horizontal plane since the behavior in the vertical plane is practically identical, due to the symmetry of the e-cloud distribution (see Fig. 1).

The instabilities are studied in particular as a function of the RF voltage settings, since a reduction of the RF voltage is being considered for future LHC operation in order to cope with RF power limitations. The RF voltage setting affects the bunch length of the circulating bunches. The bunch length measured at the LHC after injection and filamentation with different RF voltages are shown in Fig. 2 [12]. A linear fit is applied to the data and used to set the bunch length in the simulations depending on the chosen voltage. The longitudinal distribution of the bunch is matched to the non-linear RF bucket.

Unless differently stated, the Secondary Electron Yield (SEY) parameter ($\delta_{\max}$ [13]) is assumed equal to 1.3. In some cases, the value SEY = 1.4 is considered to study the effect of a stronger e-cloud.

3.1 Numerical convergence studies

We have studied the numerical convergence properties of the simulations with respect to the following numerical parameters:

- the number of longitudinal slices along the bunch, which defines the discretization of the beam charge profile and the integration time step for the electron motion;
- the configuration of the transverse grids used to compute the fields generated by the beam and by the electrons through the PIC method.

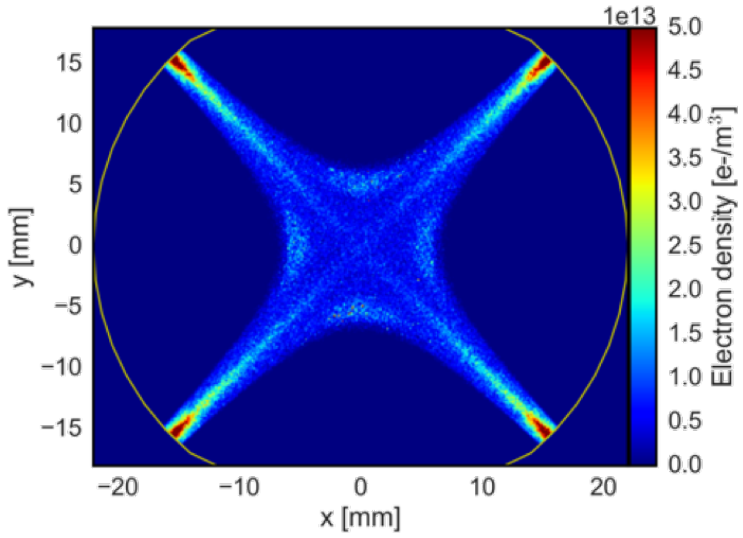

Figure 1: Electron distribution in the LHC arc quadrupoles at injection energy as seen right before the arrival of a bunch (from PyECLOUD buildup simulation).

- the average number of MPs per slice used to model the proton bunch;
- the number of MPs used to model the e-cloud at each interaction;
- the number of e-cloud interactions along the ring.

Since it would be prohibitive to perform simulations for all possible combinations, we scanned each parameter individually using conservative settings for the others.

It is worth underlying that, in each simulation, the MP distribution for the proton bunch is stochastically generated. This introduces visible fluctuations on the behavior of the instability.

3.1.1 Longitudinal slicing of the proton bunch

The number of longitudinal slices along the proton bunch has been scanned between 200 and 1000, with the slicing covering the full bucket length. Simulations with different settings in this range have been performed for different values of the longitudinal parameters (RF voltage and corresponding bunch length, as defined in Sec. 1). The instability growth observed in the different simulations is reported in Fig. 3 (a). Numerical convergence is observed when the number of slices is larger than 300.

The number of longitudinal slices, has a strong impact on the required computational time, as illustrated in Fig. 3 (b).

To understand the origin of such requirements in terms of longitudinal slicing, we analyzed the motion of individual electrons at small transverse amplitude, as in this case the oscillation of the electron in the beam potential can be expressed analytically [14, 15]. In Fig. 4 (a), we observe that when using a too small number of slices, the amplitude of the electron oscillation artificially increases along the bunch. This effect is instead suppressed for a sufficiently large number of slices as shown in Fig. 4 (b) (the small discrepancy that is still observed is due

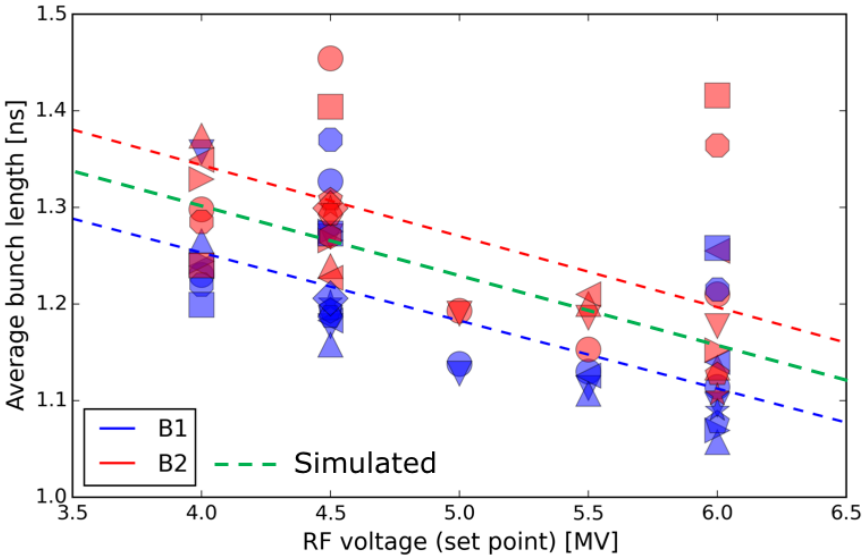

Figure 2: Bunch length as a function of the RF voltage as measured at the LHC (dots). The blue and red lines show a linear fit of the data for the two beams separately. The green line is the average between the two beams [12].

to the fact that the magnetic field is neglected in the analytical calculation). When the number of slices is too small, the inaccurate modeling of the electron motion results in a reduced electron density at the beam location, as illustrated in Fig. 5. This, in turn, tends to artificially stabilize the bunch as observed in Fig. 3 (a).

In PyECLOUD each time-step is divided in a certain number of substeps in which the electric fields are kept constant. This is convenient to handle the very fast cyclotron motion of the electrons in the presence of strong magnetic fields. In instability simulations this is done based on the input parameter Dt_{REF} which defines the target size of these substeps. In the simulations described in this document Dt_{REF} is set to 5 ps. Recently the possibility of updating also the electric fields at each substep has been introduced in PyECLOUD (as of version 8.3.0). This is done without performing the full PIC recalculation, but simply re-interpolating the field map at the new MP location at each substep. This is found to significantly improve the convergence properties as shown in Fig. 6 (a), but implies some cost in terms of computing time, especially for small numbers of slices, as it is visible comparing Fig. 6 (b) against Fig. 3 (b). This mode has not been used for the simulation studies presented in the following, as it was introduced only recently, but it is recommended for future studies.

3.1.2 Transverse grid configuration

PyECLOUD offers the possibility of using multiple grids for the computation of the fields (generated by the beam and by the electrons) with different resolutions in different portions of the chamber [5, 16]. For the simulations discussed in this section we use a coarser grid covering the entire chamber together with a finer grid covering a small region around the beam. This allows getting a better accuracy on the forces acting on the bunch while keeping a reasonable computational cost.

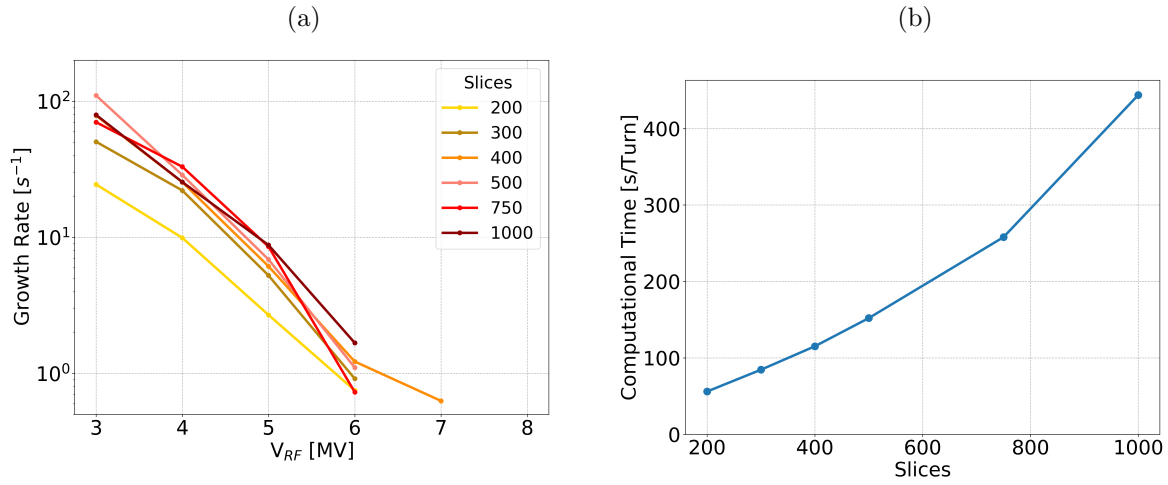

Figure 3: (a) Instability growth rate as a function of the RF voltage for different numbers of longitudinal slices. (b) Dependence of the computation time on the number of longitudinal slices.

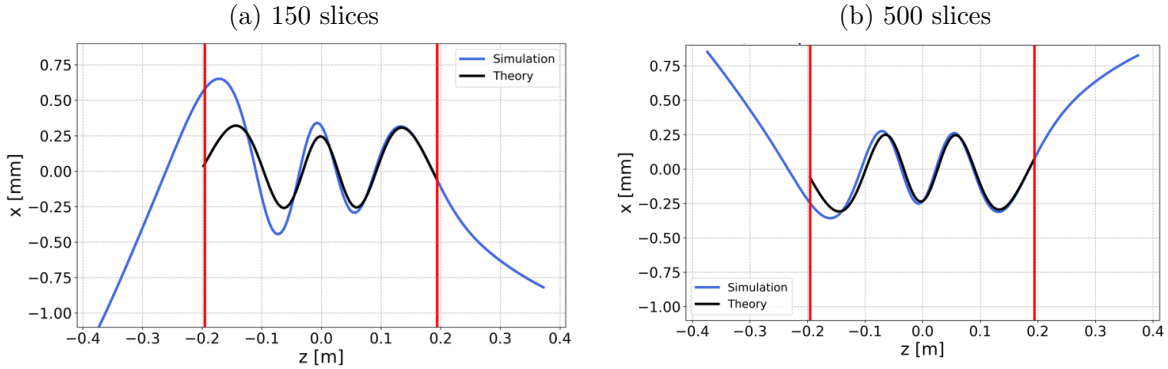

Figure 4: Comparison between the simulated and analytical oscillation of low-amplitude electrons. The simulation is performed with 150 longitudinal slices (a) and with 500 longitudinal slices (b). The z coordinate is defined such that $z > 0$ corresponds to the head of the bunch.

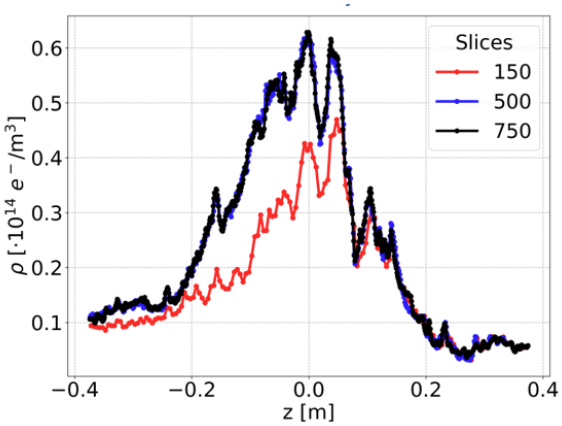

Figure 5: Electron density at the bunch location from simulations performed with different numbers of slices. The z coordinate is defined such that $z > 0$ corresponds to the head of the bunch.

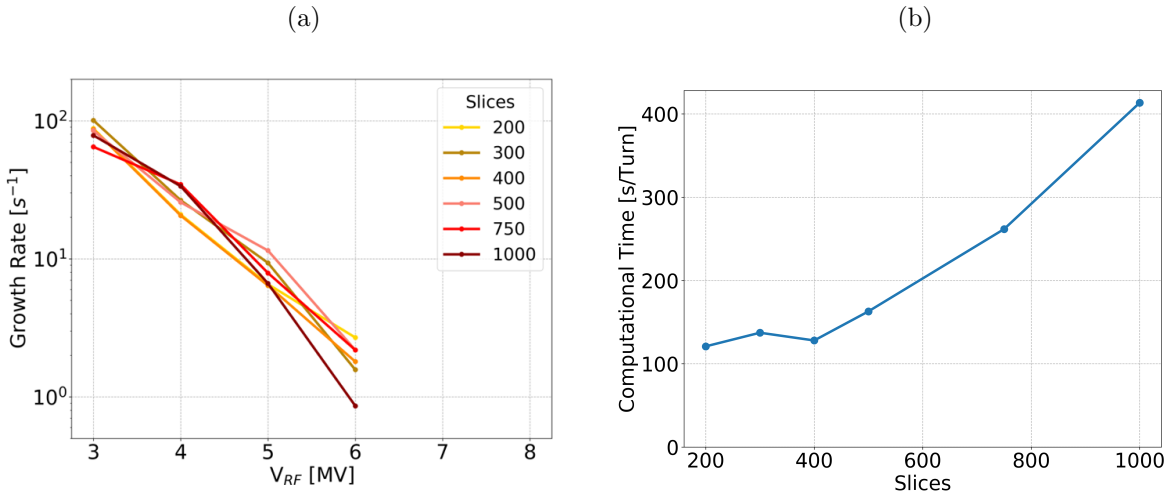

Figure 6: (a) Instability growth rate as a function of the RF voltage for different numbers of longitudinal slices, using the electric field re-interpolation at each substep. (b) Dependence of the computation time on the number of longitudinal slices, using the electric field re-interpolation at each substep.

.

To validate the transverse grid configuration, we compared simulations performed with the same settings as in past studies [6], which will be called T_0 in the following, against more conservative configurations called $T_{inj,1}$, $T_{inj,2}$, and $T_{inj,3}$, which feature smaller cell sizes both for the internal and the external grid and a larger extension of the internal grid. The parameters of the tested grid configurations are reported in Tab. 2.

Table 2: Parameters of the tested transverse grid configurations. The cell size for the external grid is defined in millimeters, while the extension and the cell size of the internal grid are defined with respect to the transverse r.m.s. beam size σ.

	T_0	$T_{inj,1}$	$T_{inj,2}$	$T_{inj,3}$
external grid cell size	0.8 mm	0.4 mm	0.4 mm	0.4 mm
internal grid extension	$\pm 10\,\sigma$	$\pm 15\,\sigma$	$\pm 15\,\sigma$	$\pm 15\,\sigma$
internal grid cell size	$0.2\,\sigma$	$0.2\,\sigma$	$0.1\,\sigma$	$0.05\,\sigma$

The instability growth rate obtained from simulations performed with the different configurations is reported in Fig. 7 (a). It is found that the configuration T_0 provides sufficiently accurate estimates and can be used for production studies. Figure 7 (b) shows the impact of the grid configuration on the required computational time.

3.1.3 Number of macroparticles

The convergence properties of the simulations have been checked also with respect to the number of macroparticles used to model the e-cloud interactions and the proton bunch.

Figure 8 (a) shows the instability growth rate observed in simulations performed with different number of MPs to model the e-cloud interactions. At least 5×10^5 MPs are required

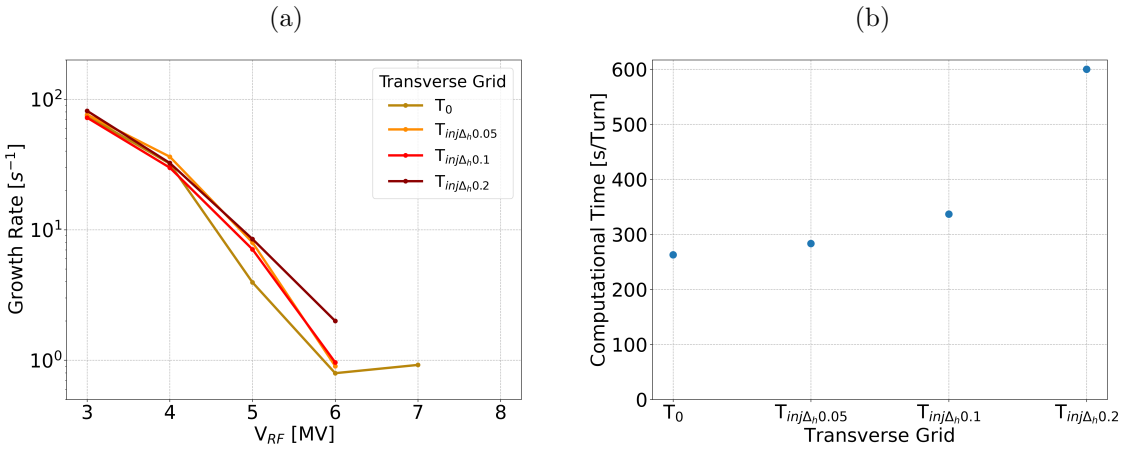

Figure 7: (a) Instability growth rate as a function of the RF voltage for different configurations of the PIC transverse grids. (b) Dependence of the computation time on the configuration of the PIC transverse grids.

to achieve convergence. The impact of this parameter on the required computational time is reported in Fig. 8 (b).

Figure 9 (a) shows the instability growth rate observed in simulations performed with different number of MPs to model the proton bunch (defined in terms of average number of macroparticles per longitudinal slice). Numerical convergence is achieved already for 10^3 MPs per slice. The impact of this parameter on the required computational time is reported in Fig. 9 (b).

3.1.4 Number of e-cloud interactions

In Fig. 10 (a), we report the growth rate obtained from simulations performed with different numbers of e-cloud interactions along the ring. Numerical convergence is obtained already with a small number of e-cloud interactions. Production studies have been performed with eight e-cloud interactions, as this also allows to mitigate emittance growth due to numerical noise, which is observed in very long simulations. The number of CPU-cores used for the simulation is chosen equal to the number of e-cloud interactions. For this reason the corresponding increase in the computational time is relatively small, as illustrated in Fig. 10, and is in line with the expectation from the employed parallelization strategy [5].

3.1.5 Selected numerical parameters

Based on the studies presented in the previous sections the configuration to be used in production studies has been defined. The selected parameters are reported in Tab. 3. Relatively conservative choices have been made when the impact on the computational time allows it.

Similar checks have also been performed for cases in which the fraction of the ring occupied by the e-cloud has been increased by a factor of two and by a factor of four. The parameters reported in Tab. 3 have been found to be valid also for these cases.

It is worth underlying that the studies presented in this section required a significant in-

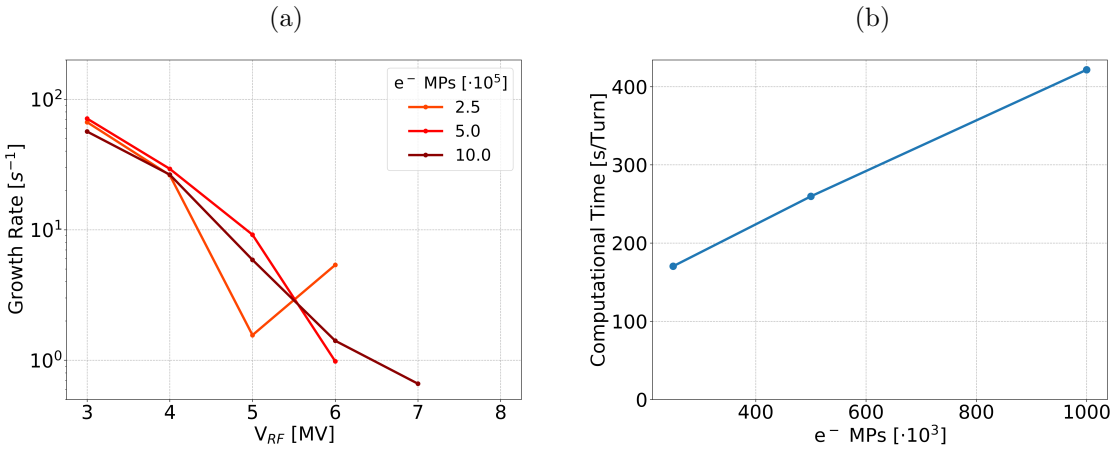

Figure 8: (a) Instability growth rate as a function of the RF voltage for different numbers of MPs at each e-cloud interaction. (b) Dependence of the computation time on the number of MPs at each e-cloud interaction.

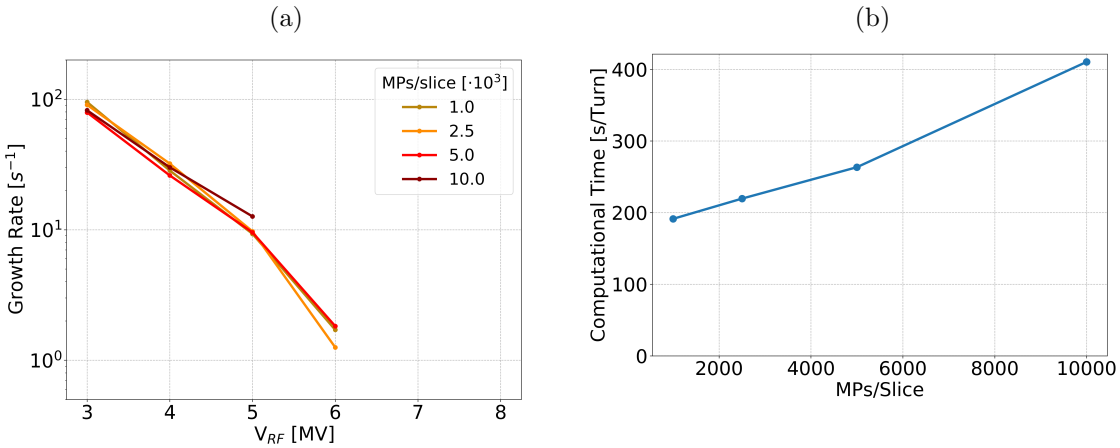

Figure 9: (a) Instability growth rate as a function of the RF voltage for different numbers of MPs used to model the bunch. (b) Dependence of the computation time on the number of MPs used to model the bunch.

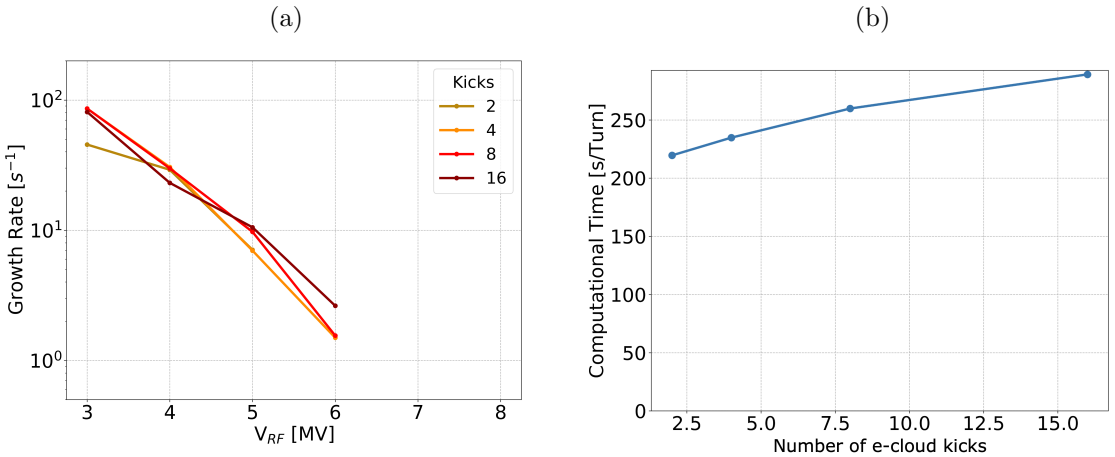

Figure 10: (a) Instability growth rate as a function of the RF voltage for different numbers of e-cloud interactions (kicks). (b) Dependence of the computation time on the number e-cloud interactions.

vestment in terms of time and computing resources. In particular 378 multi-core simulations were carried out, with a total computational time of about 32,000 CPU-cores×days. These studies required the use of a large fraction of the HPC cluster available at INFN-CNAF for several weeks.

Table 3: Parameters chosen for production studies.

Number of longitudinal slices	500
Transverse grid configuration	T_0
Number of MPs per e-cloud interaction	5×10^5
Average number of MPs per bunch-slice	2500
Number of e-cloud interactions	8

3.2 Dependence on longitudinal parameters

As already observed in the scans performed to study the numerical convergence, the instability becomes less violent when increasing the RF voltage. Figure 11 shows the same scan for two different values of the SEY. In these simulations when increasing the RF voltage the bunch length is modified based on the relation observed experimentally at the LHC (as reported in Fig. 2). The beam stability is affected in two ways: on one hand the RF voltage increase causes an increase of the synchrotron tune, which is known to affect the single-bunch stability properties [17], on the other hand the change in bunch length has an effect on the dynamics of the e-cloud, which also defines the stability properties.

To understand which of the two effects is dominant, we performed two additional sets of simulations. In the scan corresponding to the blue curve in Fig. 12 we changed the RF voltage and we kept the bunch length fixed at 1.37 ns. Conversely in the scan corresponding to the black curve in Fig. 12 we scanned the bunch length and we kept the RF voltage constant at 3 MV. It is evident that the bunch length variation has little impact on the beam stability, which is instead strongly affected by the variation in synchrotron tune driven by the voltage change.

3.3 Dependence on the bunch intensity and transverse emittance

The dependence of e-cloud effects on the bunch intensity can be non-trivial. In particular, in the LHC arc beam screens, the e-cloud buildup is expected to become weaker for large bunch intensity [11]. In fact, such a non-monotonic behavior has been recently confirmed experimentally [3].

Figure 13 shows the dependence of the electron density around the beam location as a function of the bunch intensity and of the bunch length, as obtained from PyECLOUD buildup simulations. While the dependence on the bunch length is rather mild, the effect of the bunch intensity is stronger. In particular, when the bunch intensity is increased from 1.2×10^{11} p/bunch to 2.3×10^{11} p/bunch, as foreseen for the HL-LHC upgrade [18], the electron density at the beam location is reduced by about a factor of two.

Instability simulations have been performed using the electron distributions saved from these buildup simulations with different bunch intensity. The resulting behavior of the bunch

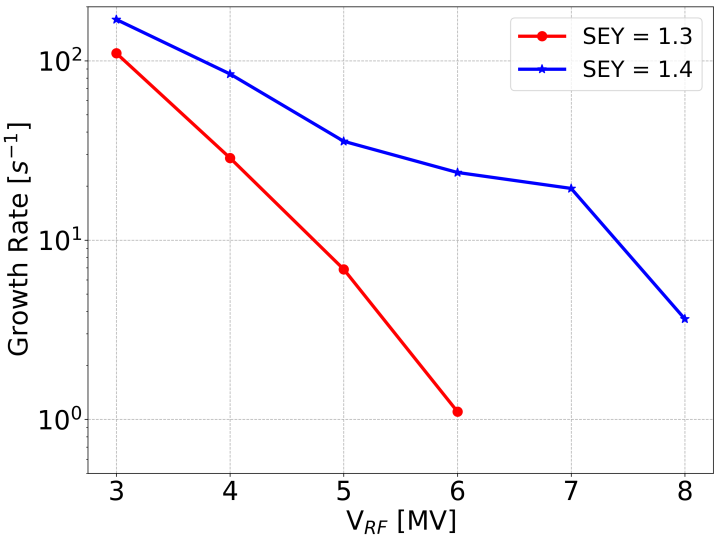

Figure 11: Instability growth rate as a function of the RF voltage for two values of the SEY.

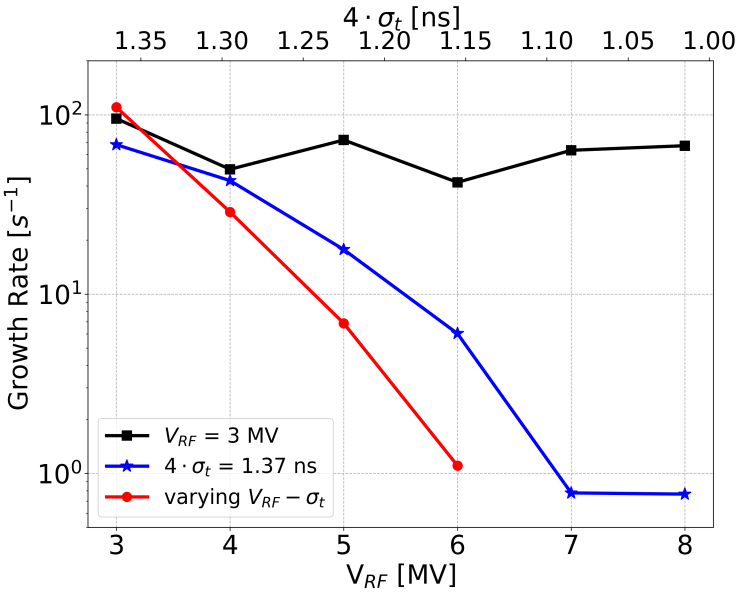

Figure 12: Instability growth rate as a function of the RF voltage and bunch length, when changing both parameters together (in red), when changing only the RF voltage (in blue), and when changing only the bunch length (in black).

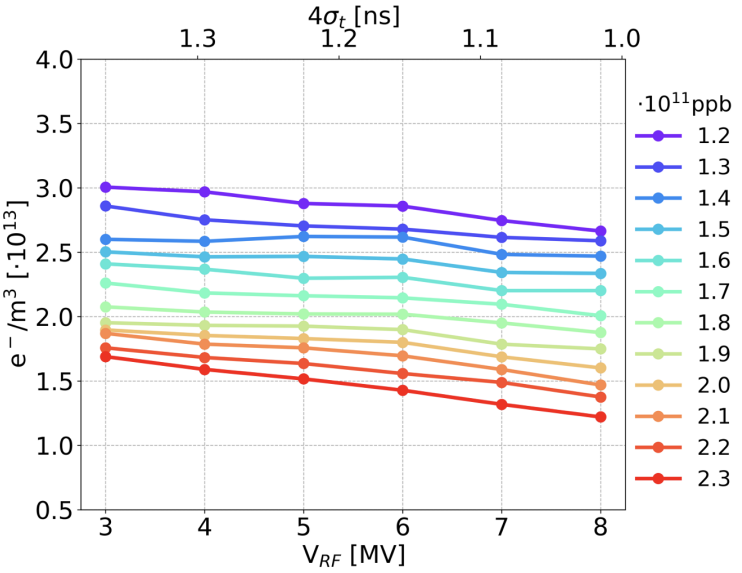

Figure 13: Electron density at the beam location as a function of the bunch intensity and the RF voltage (and corresponding bunch length), as obtained from PyECLOUD buildup simulations.

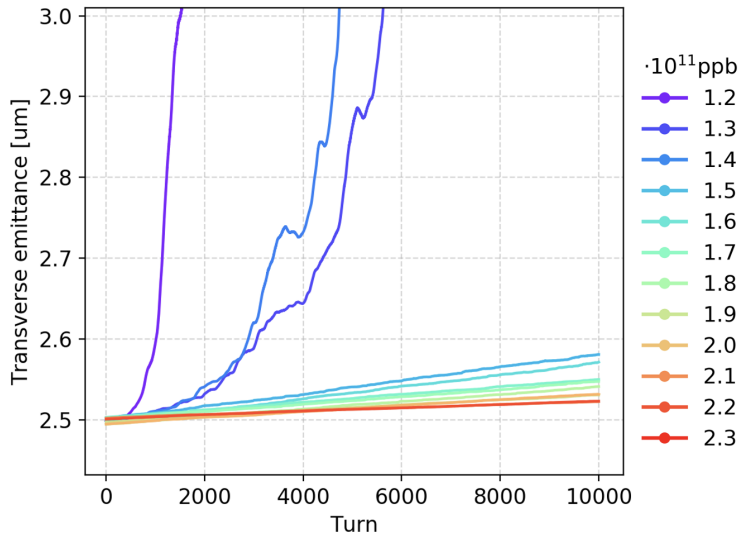

Figure 14: Evolution of the transverse emittance from instability simulations performed for different bunch intensities.

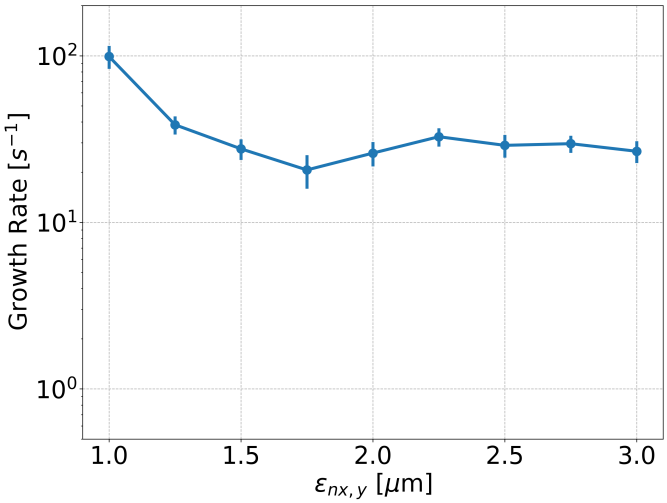

Figure 15: Instability growth rate as a function of the normalized emittance for a bunch intensity of 1.2×10^{11} p/bunch, SEY = 1.4, $V_{RF} = 6$ MV.

for the RF voltage $V_{RF} = 6$ MV is illustrated in Fig. 14. Over the simulated 10^4 turns, an instability could be observed only for the lower values of the bunch intensity.

The dependence of the instability behavior on the bunch transverse emittance has also been investigated. Figure 15 shows the growth rate as a function of the transverse emittance for a bunch intensity of 1.2×10^{11} p/bunch, SEY = 1.4, $V_{RF} = 6$ MV. The observed dependence is rather weak. In fact, in order to distinguish the effect of the transverse emittance from statistical fluctuations due to the generation of the bunch distribution, we needed to simulate each case twenty times. In the plot we report the average growth rate (dots) and the standard deviation observed over the twenty repetitions (error-bars).

3.4 Effect of transverse damper, chromaticity, and octupoles

We have also investigated in simulation the effectiveness of different tools that can be used in operation to mitigate these instabilities, in particular the transverse feedback system (damper) together with different chromaticity and octupole settings.

In Fig. 16 we study the effect on the instability growth rate of different chromaticity settings with and without the transverse damper, in the absence of octupoles. These simulations have been performed for a bunch intensity of 1.2×10^{11} p/bunch and $V_{RF} = 4$ MV. The instability growth rate is strongly reduced for large positive chromaticity. In fact, over the simulated 2×10^4 turns, no instability could be observed for Q'>15 both for SEY = 1.3 and for SEY = 1.4.

For the case SEY = 1.3 the chromaticity scan has been repeated with and without the transverse damper (the feedback damping time is chosen equal to ten turns). The damper is observed to have very little effect on the instability growth rate. This is due to the fact that the instability shows a strong intrabunch motion (as will be discussed in Sec. 3.5), which

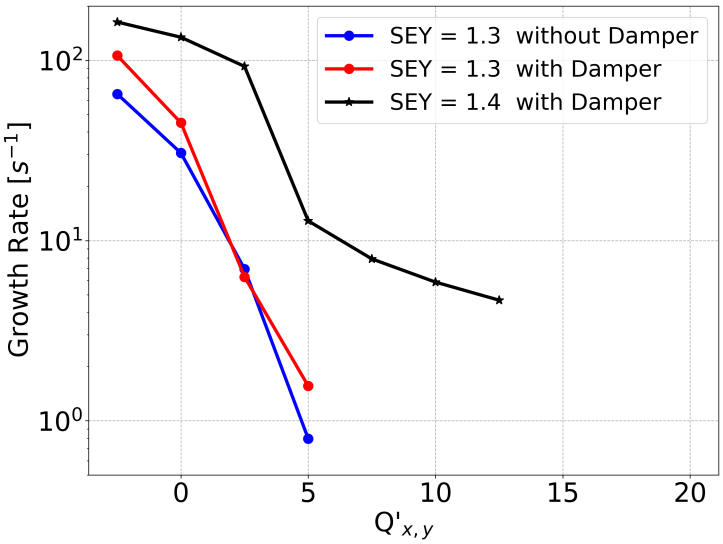

Figure 16: Instability growth rate as a function of the chromaticity for $V_{RF} = 4\,\mathrm{MV}$, a bunch intensity of $1.2{\times}10^{11}$ p/bunch and two different values of the SEY. In the case SEY = 1.3, the simulations have been performed with and without the transverse damper.

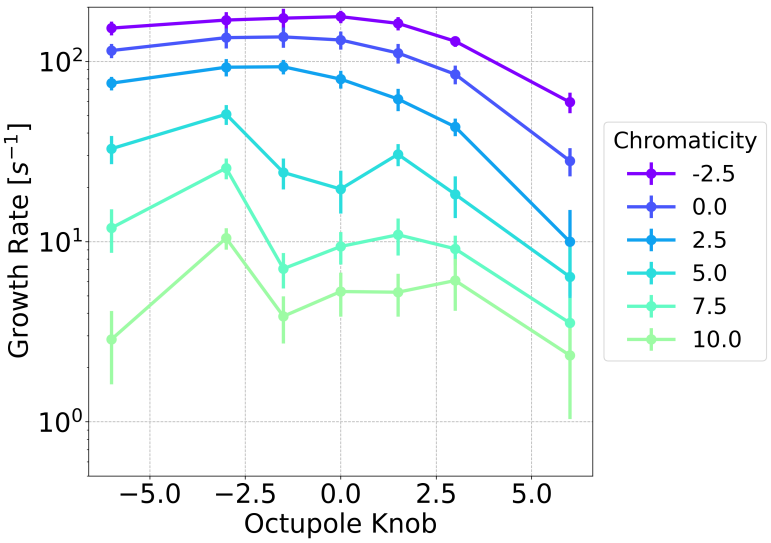

Figure 17: Instability growth rate as a function fo the octupole strength for different values of the chromaticity, for the case $V_{RF} = 4\,\mathrm{MV}$, SEY = 1.4 and a bunch intensity of $1.2{\times}10^{11}$ p/bunch.

cannot be damped by the conventional bunch-by-bunch feedback installed in the LHC.

In Fig. 17 we analyze the effect of the octupoles on the instabilitity growth rate considering the case $V_{RF} = 4\,\mathrm{MV}$, SEY = 1.4 and a bunch intensity of $1.2{\times}10^{11}$ p/bunch. The octupole knob[1] has been scanned between -6 and +6 for different values of the chromaticity. As the effect is not very pronounced, each simulation point has been repeated 20 times in order to distinguish the effect of the octupoles from fluctuations related to the generation of the bunch MP distribution. The effect of the octupoles is indeed visible but not very strong. The dependence on the knob value is non monotonic, especially for high chromaticities. Large values of the octupole knob tend to reduce the instability growth rate, especially when the sign of the knob is positive.

3.5 Intrabunch motion and frequency analysis

The single-bunch instabilities discussed so far are often characterized by the absence of a clear growth in the motion of the bunch centroid, as illustrated in Fig. 18 (a). The instability is instead revealed by the development of a strong intrabunch motion, as illustrated in Fig. 19, accompanied by fast transverse emittance blow-up.

To better understand the spectral properties of the instability, at each turn we apply a Fourier transform to the position along the bunch recorded by PyHEADTAIL, obtaining the spectrogram reported in Fig. 18 (b). The resulting "intrabunch" frequency is expressed in terms of number of oscillations N_{osc} over the full bunch length ($4\sigma_z$). The spectral line corresponding to a rigid oscillation of the bunch ($N_{\mathrm{osc}} = 0$) shows indeed a decreasing amplitude. Instead, an increase in amplitude is observed on other spectral lines in particular in the range $0.5 < N_{\mathrm{osc}} < 2.5$. The time evolution of the sine and cosine components of the strongest spectral line is illustrated in Fig. 18 (c), where the development of the instability is clearly visible.

By performing a double Fourier transform with respect to the intrabunch position and with respect to time, we obtain the 2D spectrum reported in Fig. 20. The vertical dashed line indicates the unperturbed betatron tune. A positive tune shift is observed on the rigid-bunch line ($N_{\mathrm{osc}} = 0$) while the unstable lines ($0.5 < N_{\mathrm{osc}} < 2.5$) show a negative tune shift. Recent work based on a linearized model of the e-cloud has shown that the instability is generated by a Transverse Mode Coupling mechanism [8].

Having identified the frequency of the unstable line is useful to explain why the octupoles are ineffective for suppressing the instability. Figure 21 (a) shows the tune footprint generated by the octupoles alone for the case of a strong positive amplitude detuning ($K_{\mathrm{OCT}} = -6$). In this case the tune spread overlaps with the unstable line (indicated in red).

The e-cloud alone generates the footprint reported in Fig. 21 (b) introducing a positive detuning both in the horizontal and in the vertical plane. The combined effect of octupoles and e-cloud on the footprint is shown in Fig. 21 (d) and the corresponding particle density in the horizontal tune space is reported in Fig. 21 (c). We observe that, due to the positive detuning introduced by the e-cloud, the particle density in the tune space at frequencies

[1]The operational octupole knob K_{OCT} at the LHC is defined such that, at injection energy, the current in the *LOF* octupole magnets is given by $I_{\mathrm{LOF}} = -K_{\mathrm{OCT}} \times (13\,A)$ and the current in the *LOD* octupole magnets is opposite. The relations giving the corresponding amplitude detuning coefficients can be found in [19].

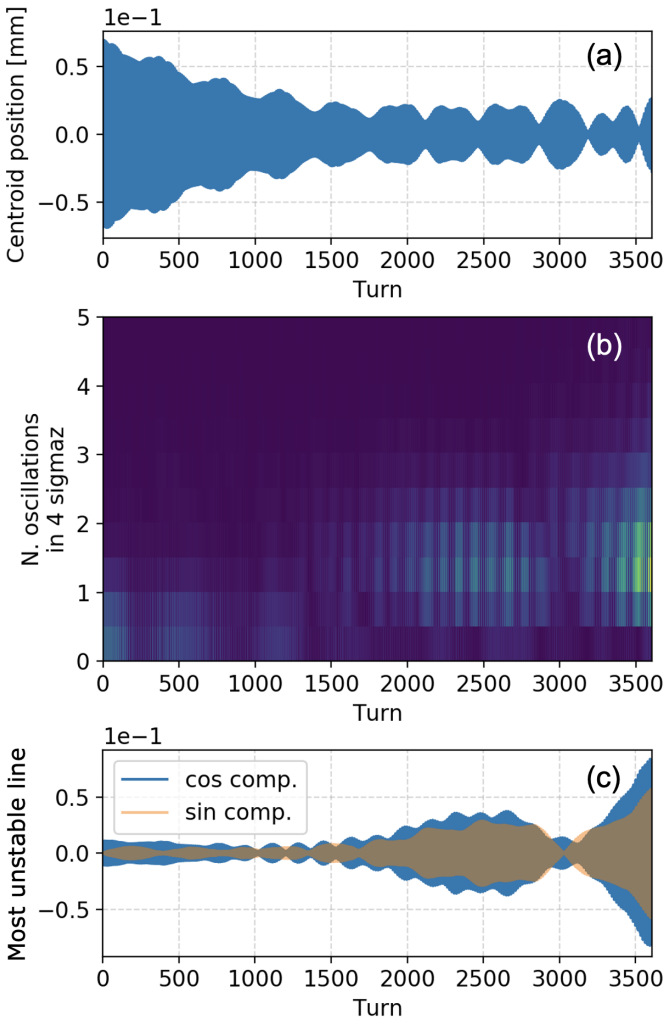

Figure 18: Evolution of the bunch centroid position (a), of the intrabunch spectrum (b) and of the most unstable intrabunch spectral line (c), for a case with $V_{RF} = 5\,\mathrm{MV}$, SEY $= 1.3$, 1.2×10^{11} p/bunch.

close to the unstable line is very low, rendering Landau damping ineffective. The fact that the e-cloud detuning shifts the tune spread away from the unstable spectral line is clearly shown in Fig. 22.

The figures reported in this section refer to the case $V_{RF} = 5\,\mathrm{MV}$. Similar features are found for all values of V_{RF} in the considered range [20].

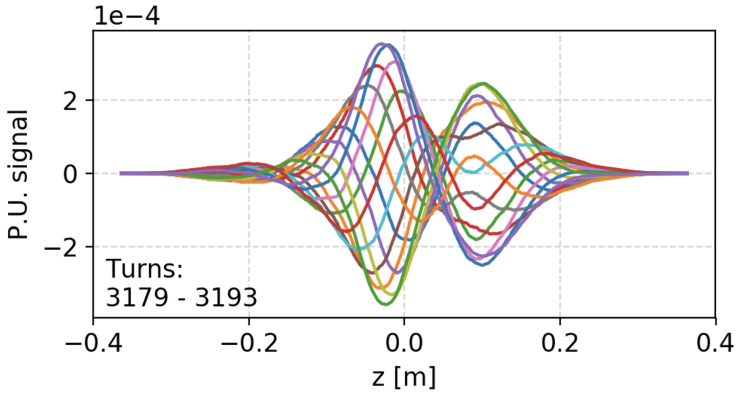

Figure 19: Intrabunch motion from the simulation reported in Fig. 18. The z coordinate is defined such that $z > 0$ corresponds to the head of the bunch.

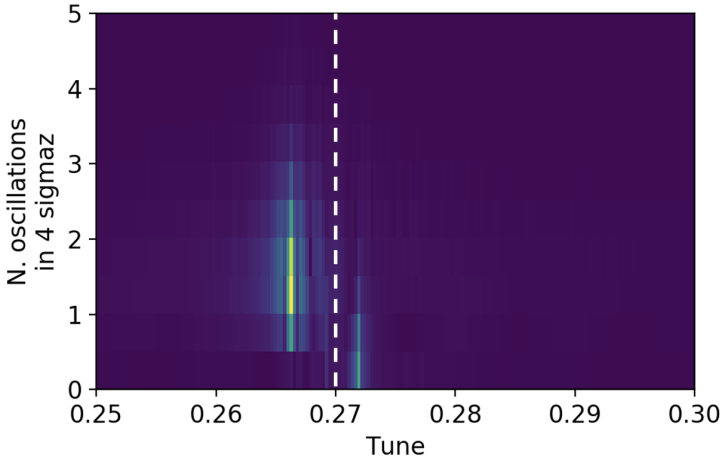

Figure 20: 2D spectrum obtained by applying a double Fourier transform to the intrabunch motion for the simulation reported in Fig. 18. The vertical dashed line marks the unperturbed betatron tune.

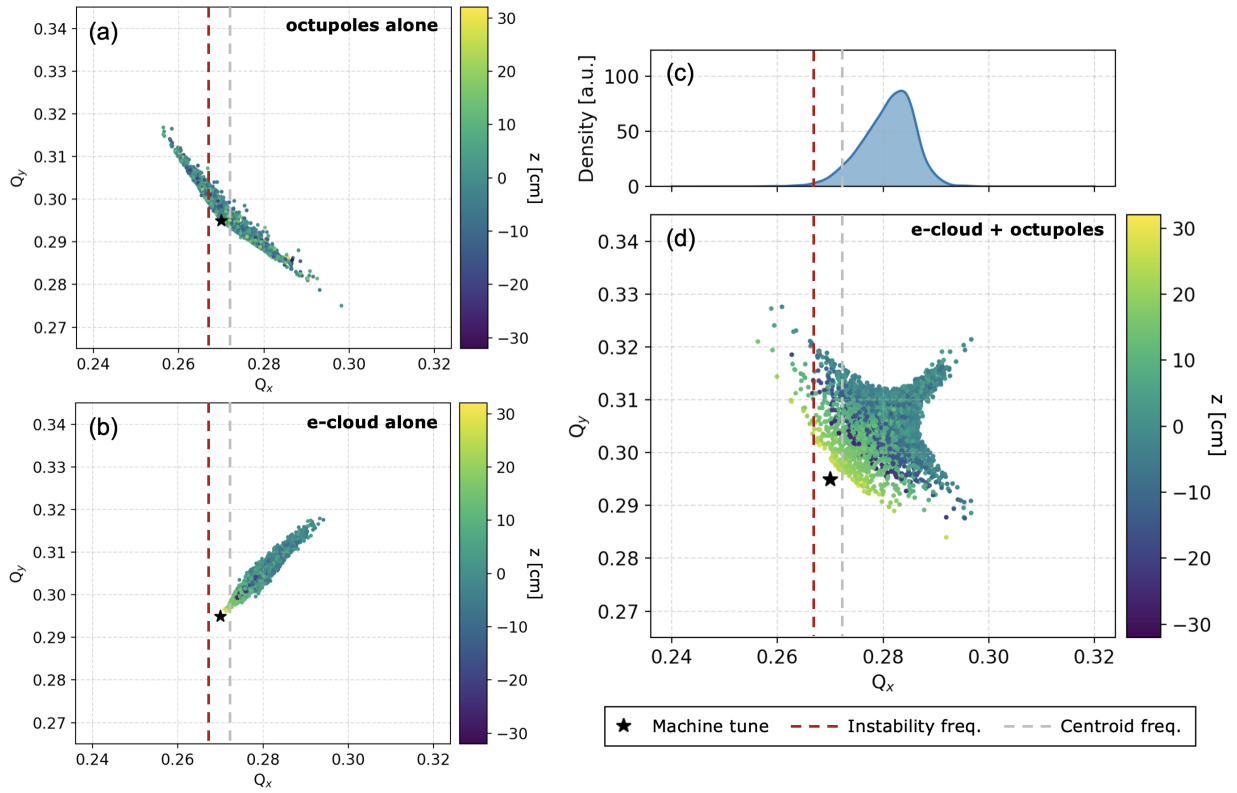

Figure 21: Tune footprints accounting for the effect of the octupoles alone (a), for the effect of the e-cloud alone (b), and for the effect of the two together (d). For the latter the corresponding particle density in the horizontal tune space is also reported (c).

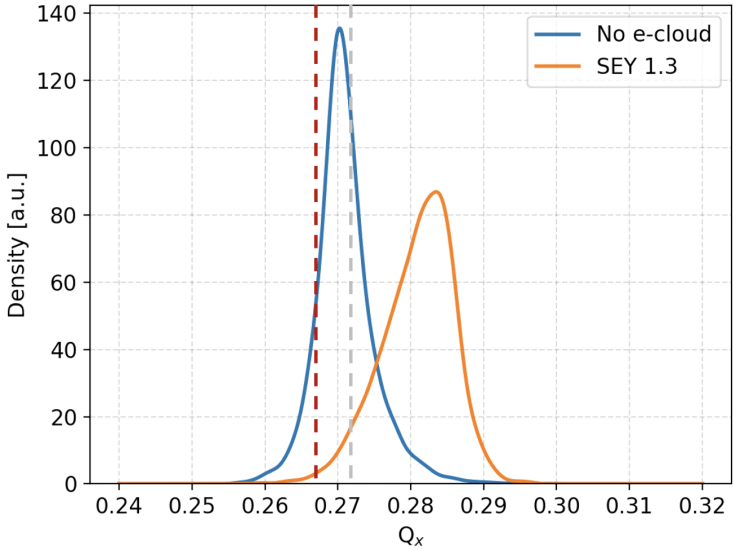

Figure 22: Comparison between the tune spread introduced by the octupoles alone (K_{OCT} = -6.0) and by the octupoles and the e-cloud together. The red dashed line marks the frequency of the unstable line, the grey dashed line marks the frequency of the centroid oscillation.

4 Instabilities driven by e-cloud in the quadrupoles at collision energy

From previous simulation studies, instabilities driven by e-cloud in the LHC are expected to be less critical at collision energy compared to injection energy (mainly because the e-cloud kicks become weaker due the increased beam rigidity) [6]. We have performed a set of convergence scans for this simulation scenario, studying in particular the dependence of the instability growth rate on the beta function at the e-cloud interactions (for simplicity the beam is assumed to be round at those locations).

As for the low-energy case, the convergence properties have been studied with respect to the number of longitudinal slices, the transverse grid configuration, the number of MPs used to model the e-cloud and the bunch, and the number of e-cloud interactions. In the simulations, the SEY parameter is assumed equal to 1.3. The obtained growth rate and the computation time for the different simulated configurations are reported in Figs. 23 - 27.

One important difference with respect to the injection-energy scenario is that at collision energy the transverse beam size is much smaller. As a consequence the cell size of the internal grid needs to be significantly smaller as well. For this reason, as set of nested grids is used to smoothly match the coarse external grid covering the entire chamber with the fine grid required to resolve the beam [5, 16]. The different grid configurations that have been tested are reported in Tab. 4. By default the internal grid sizes change when scanning the beta function, as they are defined with respect to the transverse beam size. A configuration called T_B, in which the same grid sizes are used for all simulations, has also been tested. Tests have been performed also with a configuration called T_S without multiple grids, in which the cell size of the main grid is chosen small enough to resolve the beam (this results in a very high computational burden compared to the multi-grid cases, as shown in Fig.24 (b)).

As a result of the convergence scans, the numerical parameters reported in Tab. 5 are recommended for future studies in collision-energy configurations.

Table 4: Parameters of the tested transverse grid configurations. The cell size for the external grid is defined in millimeters, while the extension and the cell size of the internal grid are defined with respect to the transverse r.m.s. beam size σ.

	T_0	T_1	T_2	T_B	T_S
external grid cell size	0.8 mm	0.4 mm	0.4 mm	0.8 mm	3.5×10^{-5} mm
internal grid extension	$\pm10\,\sigma$	$\pm10\,\sigma$	$\pm10\,\sigma$	$\pm10\,\sigma_{\max}$	n.a.
internal grid cell size	$0.2\,\sigma$	$0.2\,\sigma$	$0.1\,\sigma$	$0.2\,\sigma_{\min}$	n.a.

Table 5: Parameters chosen for collision-energy studies.

Number of longitudinal slices	750
Transverse grid configuration	T_0
Number of MPs per e-cloud interaction	5×10^5
Average number of MPs per bunch-slice	2500
Number of e-cloud interactions	4

As it can be seen from Figs. 23 - 27 no instabilities are observed over the simulated 2×10^4 turns for values of the beta function below 400 m. For all scenarios considered for LHC operations and for the HL-LHC upgrade [18] the average beta function in the arcs is well below such a value.

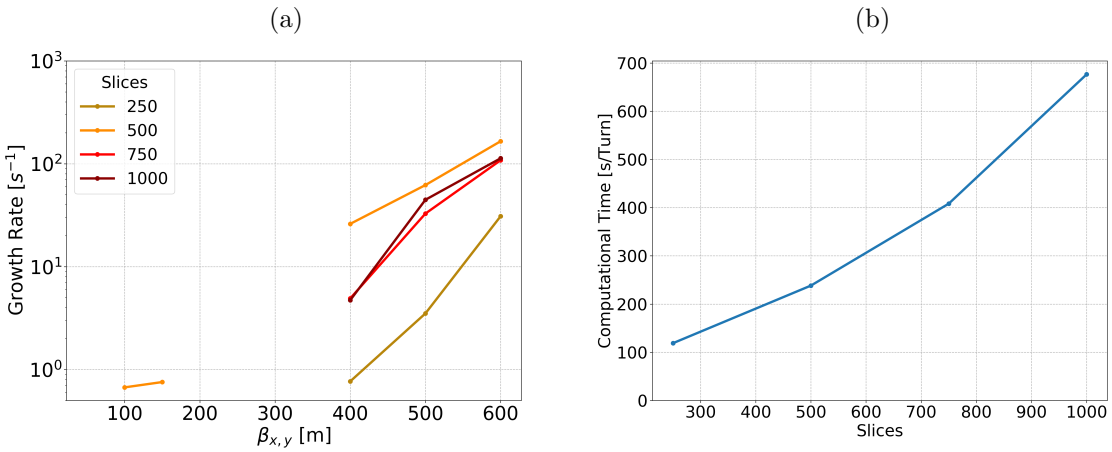

Figure 23: (a) Instability growth rate as a function of the beta function at the e-cloud interactions for different numbers of longitudinal slices. (b) Dependence of the computation time on the number of longitudinal slices.

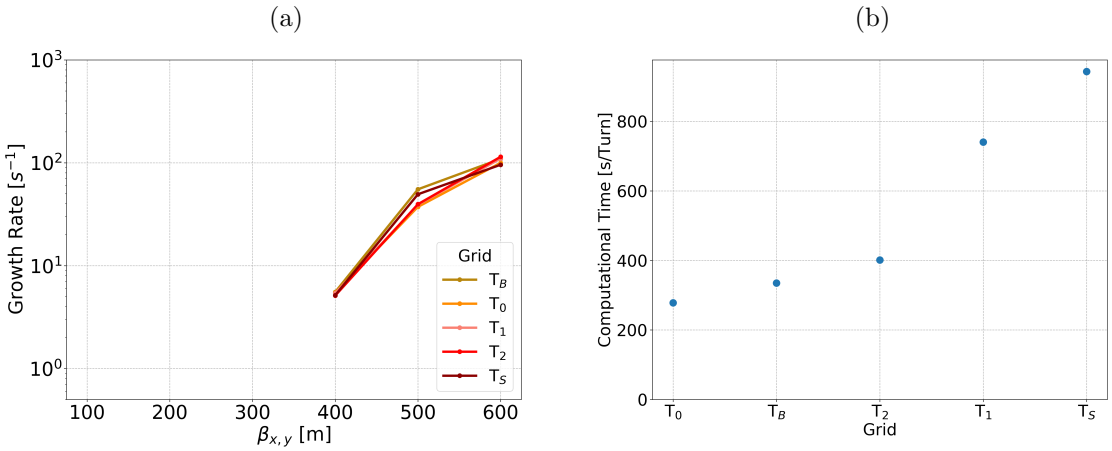

Figure 24: (a) Instability growth rate as a function of the beta function at the e-cloud interactions for different for different configurations of the PIC transverse grids. (b) Dependence of the computation time on the configuration of the PIC transverse grids.

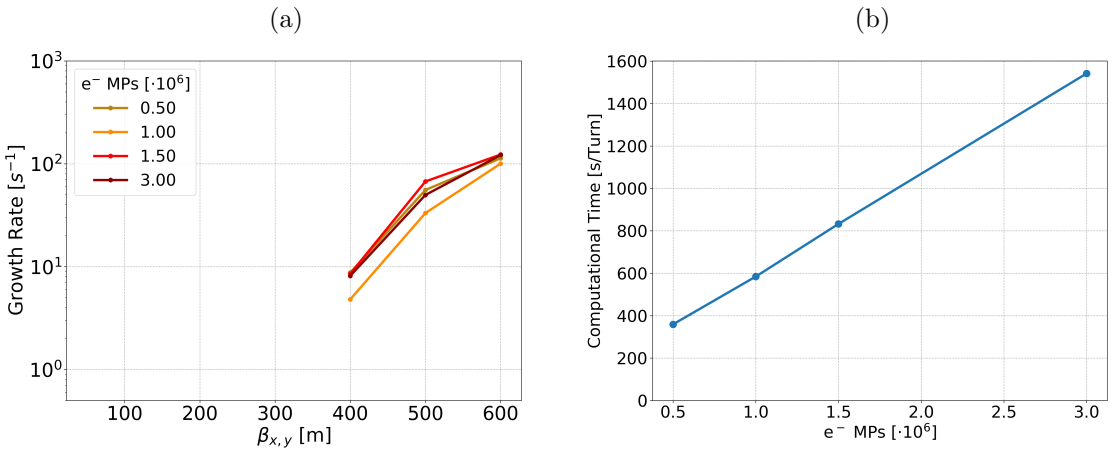

Figure 25: (a) Instability growth rate as a function of the beta function at the e-cloud interactions for different numbers of MPs at each e-cloud interaction. (b) Dependence of the computation time on the number of MPs at each e-cloud interaction.

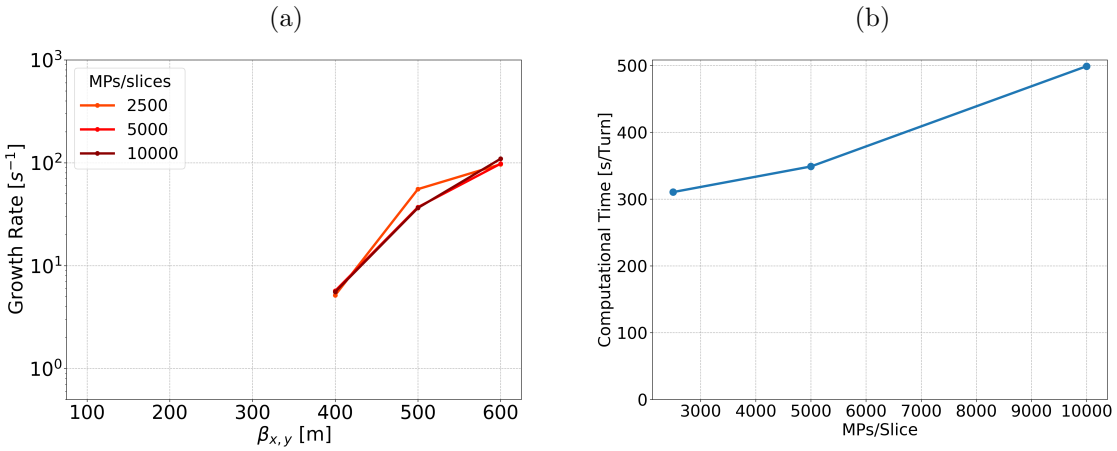

Figure 26: (a) Instability growth rate as a function of the beta function at the e-cloud interactions for different numbers of MPs used to model the bunch. (b) Dependence of the computation time on the number of MPs used to model the bunch.

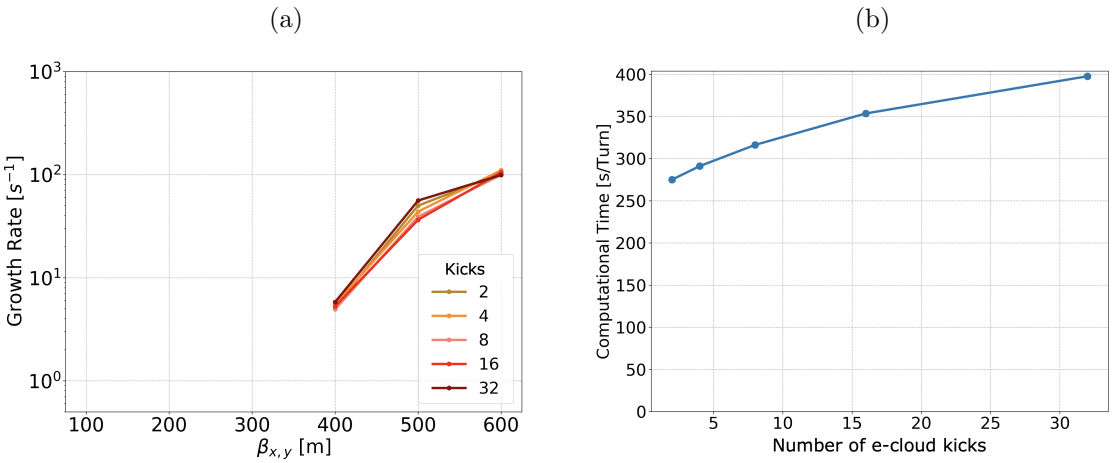

Figure 27: (a) Instability growth rate as a function of the beta function at the e-cloud interactions for different numbers of e-cloud interactions (kicks). (b) Dependence of the computation time on the number e-cloud interactions.

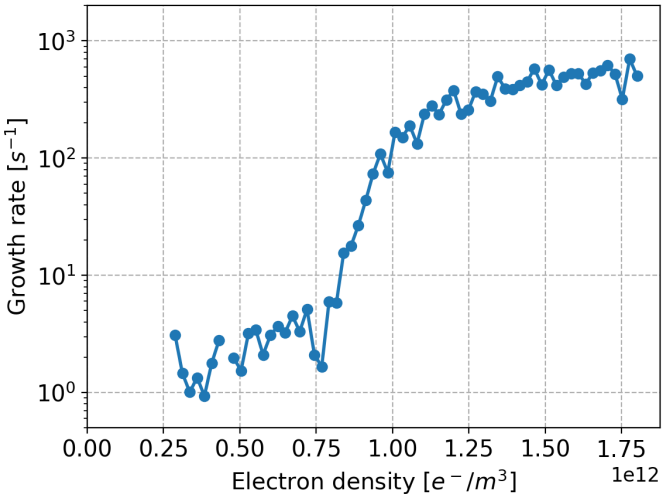

Figure 28: Instability growth rate as a function of the e-cloud density in the dipole magnets.

5 Instabilities driven by e-cloud in the dipoles at injection energy

Although e-cloud in the dipole magnets is a less strong source for single-bunch instabilities compared to the quadrupole case, we performed a set of simulations to investigate its effect, also in view of comparisons against a newly developed linearized model [8].

The numerical parameters of the simulations were configured based on the convergence studies presented in Sec. 3.1. The beam stability in the vertical plane was studied as a function of the electron density at the beam location. The obtained growth rate as a function of the electron density is reported in Fig. 28. No instability is observed for electron densities below $2.5\times10^{12}\,\mathrm{e^-/m^3}$ over the simulated 2×10^4 turns. For densities between $0.25\times10^{12}\,\mathrm{e^-/m^3}$ and $0.75\times10^{12}\,\mathrm{e^-/m^3}$, a relatively slow instability is observed, while a much stronger instability appears for densities above $0.75\times10^{12}\,\mathrm{e^-/m^3}$.

The electron densities predicted in the dipoles from buildup simulations with SEY parameters below 1.4 and bunch intensities above 1×10^{11} p/bunch, are well below $0.1\times10^{12}\,\mathrm{e^-/m^3}$. Therefore these instabilities are expected indeed less critical compared to those driven by e-cloud in the quadrupoles. Instead, for values of the bunch intensity below 1×10^{11} p/bunch, the electron density at the beam location can be significantly higher, and instabilities driven by e-cloud in the dipoles are indeed possible, as observed experimentally at the LHC [21].

6 Summary and conclusions

Instabilities driven by e-cloud at the LHC have been studied by means of numerical simulations. Particular care has been given to the study of instabilities due to the e-cloud in the quadrupole magnets at injection energy. The numerical parameters of the simulations have been defined through extensive convergence studies which are also meant to provide useful guidelines for future simulation campaigns. The stability properties have been studied in particular with repect to the RF voltage settings. The beam is found to be more stable for higher voltage as a result of the faster synchrotron motion.

Increasing the bunch intensity is found to mitigate the instability as result of the fact that the electron density becomes lower. A bunch-by-bunch damper is found to be unable to suppress the instability due to the presence of a strong intrabunch motion. Octupole magnets are also found to be rather ineffective, due to the fact that the detuning forces due to the e-cloud tend to move the tune spread away from the frequency of the observed unstable mode. The instability can instead be suppressed using large chromaticity settings.

Simulations have also been performed for instabilities driven by e-cloud in the quadrupoles at collision energy. The simulations confirm no instability is expected at collision energy in the operational conditions foreseen for LHC and HL-LHC.

Instabilities driven by e-cloud in dipole magnets at injection energy were also simulated, confirming that they are not expected to be critical for realistic values of the bunch intensity and of the SEY.

Acknowledgements

The simulation studies discussed in this note were performed on the High Performance Computing cluster at INFN-CNAF in Bologna (Italy). The authors would like to thank G. Arduini, D. Cesini A. Falabella, G. Maron, E. Métral, A. Romano, G. Rumolo for their input and support to the presented studies.

References

[1] G. Iadarola, G. Rumolo, P. Dijkstal, and L. Mether, "Analysis of the beam induced heat loads on the LHC arc beam screens during Run 2," *CERN-ACC-NOTE-2017-0066*, Dec 2017.

[2] G. Iadarola *et al.*, "Electron cloud and heat loads in Run 2," *in Proc. 2019 Evian Workshop on LHC beam operation, Evian Les Bains, France*, Jan 2019. https://indico.cern.ch/event/751857/.

[3] G. Iadarola, G. Skripka, *et al.*, "Beam-induced heat loads on the LHC arc beam screens with different beam and machine configurations: experiments and comparison against simulations," *CERN-ACC-NOTE-2019-0057*, Dec 2019.

[4] X. Buffat *et al.*, "Transverse instabilities," *in Proc. 2019 Evian Workshop on LHC beam operation, Evian Les Bains, France*, Jan 2019. https://indico.cern.ch/event/751857/.

[5] G. Iadarola, E. Belli, K. Li, L. Mether, A. Romano, and G. Rumolo, "Evolution of python tools for the simulation of electron cloud effects," *in Proc. 8th International Particle Accelerator Conference, Copenhagen, Denmark*, May 2017. pp.THPAB043.

[6] A. Romano, "Electron cloud formation in CERN particle accelerators and its impact on the beam dynamics," *CERN-THESIS-2018-299*, 2018.

[7] R. J. Macek *et al.*, "Electron cloud generation and trapping in a quadrupole magnet at the Los Alamos proton storage ring," *Phys. Rev. Accel. Beams*, vol. 11, no. 1, p. 010101, 2008.

[8] G. Iadarola, L. Mether, N. Mounet, and L. Sabato, "Linearized method for the study of transverse instabilities driven by electron clouds," *Phys. Rev. Accel. Beams*, vol. 23, p. 081002, Jul 2020.

[9] R. W. Hockney and J. W. Eastwood, *Computer simulation using particles*. crc Press, 1988.

[10] G. Iadarola, "Modelling the interaction of a relativistic beam particle with an electron cloud," *CERN-ACC-NOTE-2019-0033*, Aug 2019.

[11] G. Skripka and G. Iadarola, "Beam-induced heat loads on the beam screens of the HL-LHC arcs," *CERN-ACC-NOTE-2019-0041*, Oct 2019.

[12] H. Timko, "Injection Voltage Reduction in the LHC," *Presentation at the LHC Machine Committee (LMC), CERN*, 5 September 2018. https://indico.cern.ch/event/755095/.

[13] G. Iadarola, "Electron cloud studies for CERN particle accelerators and simulation code development," *CERN-THESIS-2014-047*, Mar 2014.

[14] L. Sabato, "Analysis of the electron motion within the Beam," *Presentation at the Electron Cloud Meeting, CERN*, 22 February 2019.
https://indico.cern.ch/event/790352/.

[15] L. Sabato, "Single Bunch Instability Simulations: Basic Checks," *Presentation at the Electron Cloud Meeting, CERN*, 2 November 2018.
https://indico.cern.ch/event/766100/.

[16] E. Belli, "PyPIC: the Multigrid Solver," *Presentation at the Electron Cloud Meeting, CERN*, 2 September 2016.
https://indico.cern.ch/event/547910/.

[17] H. Bartosik, "Beam dynamics and optics studies for the LHC injectors upgrade," *CERN-THESIS-2013-257*, Oct 2013.

[18] E. Métral *et al.*, "Update of the HL-LHC operational scenarios for proton operation," *CERN-ACC-NOTE-2018-0002*, Jan 2018.

[19] N. Mounet, "The LHC Transverse Coupled-Bunch Instability," *CERN-THESIS-2012-055*, Mar 2012.

[20] G. Iadarola, "Indications from frequency analysis," *Presentation at the Electron Cloud Meeting, CERN*, 22 November 2019.
https://indico.cern.ch/event/862794/.

[21] A. Romano, O. Boine-Frankenheim, X. Buffat, G. Iadarola, and G. Rumolo, "Electron cloud buildup driving spontaneous vertical instabilities of stored beams in the Large Hadron Collider," *Phys. Rev. Accel. Beams*, vol. 21, p. 061002, Jun 2018.